

# Formaldehyde as a Tracer of Extragalactic Molecular Gas

## I. Para-H<sub>2</sub>CO Emission From M 82<sup>1</sup>

S. Mühle and E. R. Seaquist

*Department of Astronomy and Astrophysics, University of Toronto, 50 St. George Street,  
Toronto, ON M5S 3H4, Canada*

muehle@astro.utoronto.ca, seaquist@astro.utoronto.ca

and

C. Henkel

*Max-Planck-Institut für Radioastronomie, Auf dem Hügel 69, D-53121 Bonn, Germany*

p220hen@mpifr-bonn.mpg.de

### ABSTRACT

Using the IRAM 30-m telescope and the 15-m JCMT, we explore the value of para-formaldehyde (p-H<sub>2</sub>CO) as a tracer of density and temperature of the molecular gas in external galaxies. The target of our observations are the lobes of the molecular ring around the center of the nearby prototypical starburst galaxy M 82. It is shown that p-H<sub>2</sub>CO provides one of the rare direct molecular thermometers. Reproducing the measured line intensities with a large velocity gradient (LVG) model, we find densities of  $n_{\text{H}_2} \sim 7 \times 10^3 \text{ cm}^{-3}$  and kinetic temperatures of  $T_{\text{kin}} \sim 200 \text{ K}$ . The derived kinetic temperature is significantly higher than the dust temperature or the temperature deduced from ammonia (NH<sub>3</sub>) lines, but our results agree well with the properties of the high-excitation component seen in CO. We also present the serendipitous discovery of the  $4_2 \rightarrow 3_1$  line of methanol (CH<sub>3</sub>OH) in the northeastern lobe, which shows — unlike CO and H<sub>2</sub>CO — significantly different line intensities in the two lobes.

*Subject headings:* Galaxies: individual (M 82) — galaxies: ISM — galaxies: starburst — radio lines: ISM — submillimeter — ISM: molecules

---

<sup>1</sup>Based on observations carried out with the IRAM 30-meter telescope. IRAM is supported by INSU/CNRS (France), MPG (Germany) and IGN (Spain).

## 1. INTRODUCTION

Molecular gas is regarded as the fuel for star formation. Increasing evidence for non-standard initial mass functions (e.g. Paumard et al. 2006; Klessen et al. 2007), and warm molecular gas in starburst galaxies (e.g. Rigopoulou et al. 2002; Mauersberger et al. 2003) suggest that its physical properties may influence the star formation rate and the properties of the next generation of stars. Unfortunately, the physical properties of the molecular gas in external galaxies, in particular the kinetic temperature, are often not well constrained. The easily thermalized and optically thick CO  $J = 1 \rightarrow 0$  and  $2 \rightarrow 1$  transitions could constitute a good temperature tracer, but the filling factor of extragalactic clouds is poorly constrained. Other commonly observed molecules like HCN and HCO<sup>+</sup> are good density tracers, but require an a priori knowledge of the kinetic temperature. The inversion lines of the symmetric top molecule ammonia (NH<sub>3</sub>) are frequently used as the galactic “standard cloud thermometer”. However, in the disk of the Milky Way, the fractional abundance of NH<sub>3</sub> varies between  $10^{-5}$  in hot cores (Mauersberger et al. 1987) and  $10^{-8}$  in dark clouds (Benson & Myers 1983). Thus, ammonia may trace preferentially a specific component of the molecular gas and the assumption of an approximately constant fractional abundance on linear scales of a few 100 pc is likely not valid. Other symmetric or slightly asymmetric top molecules may therefore be more favorable for extragalactic line studies.

### 1.1. Formaldehyde as a Molecular Gas Tracer

In this paper, we investigate the diagnostic properties of para-formaldehyde (p-H<sub>2</sub>CO) lines in extragalactic sources. Formaldehyde is formed on the surface of dust grains by successive hydrogenation of CO (Watanabe & Kouchi 2002), released into the gas phase by shocks or UV heating and subsequently destroyed by gas-phase processes. Variations in fractional abundance rarely exceed one order of magnitude. Johnstone et al. (2003) found only little variation in a variety of galactic environments ranging from cool protostellar candidates to hot photon-dominated regions and infrared sources with the latter showing the highest discrepancy, by a factor of 5 to 10. These higher abundances are likely caused by the release of H<sub>2</sub>CO molecules from grain surfaces in regions of massive star formation. As another example for the level of variability in the abundance of formaldehyde versus that of ammonia in active environments, the H<sub>2</sub>CO abundance is the same in the hot core and the compact ridge of Orion A, whereas the NH<sub>3</sub> abundance in the core is two orders of magnitude higher than that in the ridge (Charnley et al. 1992).

Para-formaldehyde, which is a subspecies of the slightly asymmetric top molecule H<sub>2</sub>CO, has a rich mm- and submm-spectrum of transitions. Since the relative populations of the

$K_a$  ladders are generally governed by collisions, line ratios involving different  $K_a$  ladders (inter-ladder ratios) are generally good tracers of the kinetic temperature. With the temperature known, line ratios within a single  $K_a$  ladder, the so-called intra-ladder ratios, whose populations are mainly determined by collisional excitation and radiative de-excitation, sensitively probe the gas density (Mangum & Wootten 1993). The  $K$ -doublet transitions of ortho- $\text{H}_2\text{CO}$  in the cm-range,  $1_{10} \rightarrow 1_{11}$  at  $\lambda = 6$  cm and  $2_{11} \rightarrow 2_{12}$  at  $\lambda = 2$  cm, have been observed in a number of external galaxies since the 1970s (e.g. Gardner & Whiteoak 1974; Seaquist & Bell 1990).  $\text{H}_2\text{CO}$  lines in the mm-range were detected in several galaxies including the LMC, M 82 and NGC 253 since the 1990s (e.g. Baan et al. 1990; Johansson et al. 1994), but to date there are only three published studies of the excitation conditions of extragalactic molecular gas that utilize multi-line  $\text{H}_2\text{CO}$  observations in combination with a non-LTE treatment of the radiative transfer (Hüttemeister et al. 1997; Heikkilä et al. 1999; Wang et al. 2004).

## 1.2. Target Selection: M 82

The target for our exploratory investigation is the nearby prototypical starburst galaxy M 82. As the most prominent galaxy in the northern hemisphere with a nuclear starburst, M 82 has been the target of numerous molecular line studies (e.g. Fuente et al. 2006; Seaquist et al. 2006). Most of the excitation studies focus on the central 1 kpc disk, where the molecular gas is concentrated in a circumnuclear ring around the center of the starburst (e.g. García-Burillo et al. 2002; Seaquist et al. 2006) with the more highly excited lines found at smaller radii (Fig. 1, see also Mao et al. (2000) for an overview of ring diameters). Note that the two lobes of the molecular ring in this highly inclined galaxy can be easily separated with single-dish telescopes and the observed molecular lines in the lobes have typical widths of only 100 to 150  $\text{km s}^{-1}$  (e.g. Seaquist et al. 1998; García-Burillo et al. 2002), thus greatly reducing the potential for line blending. The most comprehensive CO line studies to date (Mao et al. 2000; Ward et al. 2003) suggest that the broad data base of CO and  $^{13}\text{CO}$  lines observed towards the molecular lobes of M 82 can not be fitted by a single-component large velocity gradient (LVG) model and that the majority of the molecular gas may actually be in a high-excitation state. The  $\text{H}_2\text{CO}(1_{10} \rightarrow 1_{11})$  transition at  $\lambda = 6$  cm was detected towards the nucleus of M 82 *in absorption* by Graham et al. (1978), whereas the  $\text{H}_2\text{CO}(2_{11} \rightarrow 2_{12})$  line at  $\lambda = 2$  cm was observed *in emission*, which was interpreted as evidence for very dense ( $10^6 \text{ cm}^{-3}$ ) molecular gas in the molecular ring (Baan et al. 1990). The latter study also reported the first detection of an  $\text{H}_2\text{CO}$  emission line in the mm-range in M 82. A first multi-line  $\text{H}_2\text{CO}$  excitation study towards M 82 was performed by Hüttemeister et al. (1997, see also Sect. 1.1) using an LVG model that included 16 ortho- $\text{H}_2\text{CO}$  levels of the  $K_a = 1$

ladder.

### 1.3. Line Selection

Having developed a comprehensive LVG code for ortho-H<sub>2</sub>CO (40 levels) and para-H<sub>2</sub>CO (41 levels, see Sect. 4.1), we searched for the set of transition lines best suited for extragalactic observations while trying to minimize observational uncertainties. The usually small filling factor of extragalactic observations and the decreased sensitivity of ground-based receivers at high frequencies limits the choice to the strongest lines, usually corresponding to transitions between low excitation levels. Among the H<sub>2</sub>CO lines that can be observed with present-day receivers, the para-H<sub>2</sub>CO transitions  $3_{03} \rightarrow 2_{02}$ ,  $3_{22} \rightarrow 2_{21}$  and  $3_{21} \rightarrow 2_{20}$  stand out by being close in frequency and at the same time strong enough for extragalactic observations. With rest frequencies at 218.22 GHz, 218.48 GHz and 218.76 GHz, all three lines can be observed simultaneously, if the receiver and spectrometer both offer a bandwidth of 1 GHz. That way, the observed inter-ladder line ratio  $\text{H}_2\text{CO}(3_{03} \rightarrow 2_{02})/\text{H}_2\text{CO}(3_{21} \rightarrow 2_{20})$ , which is a good temperature tracer, will be free from uncertainties related to pointing accuracy, calibration issues or different beam widths. Due to the large line widths of extragalactic observations ( $\geq 100 \text{ km s}^{-1}$ ), the  $\text{H}_2\text{CO}(3_{22} \rightarrow 2_{21})$  line may be blended with methanol emission (see Sect. 5) and thus be of limited use for the LVG analysis. At the very high densities ( $10^6 \text{ cm}^{-3}$  Baan et al. 1990) and kinetic temperatures of 50 K to 100 K inferred for H<sub>2</sub>CO in M 82, our LVG code suggests a line ratio  $\text{H}_2\text{CO}(3_{21} \rightarrow 2_{20})/\text{H}_2\text{CO}(5_{24} \rightarrow 4_{23})$  of the order of unity, which sensitively traces the gas density. In addition, observing the  $\text{H}_2\text{CO}(3_{21} \rightarrow 2_{20})$  line with the IRAM 30-m telescope and the para-H<sub>2</sub>CO( $5_{24} \rightarrow 4_{23}$ ) line with the 15-m dish of the JCMT results in data with nearly the same beam width (11" vs. 13") and thus minimizes the uncertainty inherent in line ratios derived from observations consisting of single pointings. Using a spectrometer with a bandwidth of at least 900 MHz, the  $\text{H}_2\text{CO}(5_{24} \rightarrow 4_{23})$  transition at 363.95 GHz can be observed simultaneously with the weaker and heavily blended para-H<sub>2</sub>CO transitions  $5_{42} \rightarrow 4_{41}$  and  $5_{41} \rightarrow 4_{40}$  at 364.10 GHz as well as with the blended ortho-H<sub>2</sub>CO transitions  $5_{33} \rightarrow 4_{32}$  and  $5_{32} \rightarrow 4_{31}$  at 364.28 GHz and 364.29 GHz, respectively. The non-detection of the  $\text{H}_2\text{CO}(5_{24} \rightarrow 4_{23})$  line (see Section 3) hinted at a much lower gas density regime than previously assumed and necessitated the addition of the relatively strong para-H<sub>2</sub>CO( $2_{02} \rightarrow 1_{01}$ ) line at 145.60 GHz to the selected transitions in order to be able to derive the density-sensitive intra-ladder line ratio  $\text{H}_2\text{CO}(2_{02} \rightarrow 1_{01})/\text{H}_2\text{CO}(3_{03} \rightarrow 2_{02})$ .

Here we present the results of our para-H<sub>2</sub>CO observations. To our knowledge, this is the first dedicated search for para-H<sub>2</sub>CO transition lines of the  $K_a = 2$  ladder outside of

the Galactic neighborhood (Milky Way and Magellanic Clouds). The distribution of the H<sub>2</sub>CO emission and its correlation to other tracers will be discussed in a forthcoming paper based on high-resolution ( $\sim 4''$ ) ortho-H<sub>2</sub>CO data recently obtained with the VLA. After a description of the observations and the data reduction strategy in Sect. 2, we present the observational results in Sect. 3. In Sect. 4, we describe our LVG code and the parameter space covered, before we discuss our results and compare them to other molecular excitation studies. Finally, we report the serendipitous detection of methanol emission in one of the lobes (Sect. 5). Our conclusions are summarized in Sect. 6.

## 2. OBSERVATIONS AND DATA REDUCTION

For this study, we selected the para-H<sub>2</sub>CO transitions described in Sect. 1.3 to be observed at nearly the same spatial resolution with the IRAM 30-m telescope and the 15-m JCMT. The parameters of the observations are summarized in Table 1.

### 2.1. Observations with the IRAM 30-m Telescope

For the observations at 218 GHz, the IRAM 30-m telescope with the heterodyne receiver array HERA, consisting of nine dual-polarization receivers arranged in form of a center-filled square with a pixel separation of  $24''$ , was pointed towards the southwestern lobe (SW lobe) of M 82 at  $\alpha_{2000} = 09^{\text{h}}55^{\text{m}}49^{\text{s}}.4$ ,  $\delta_{2000} = 69^{\circ}40'43''.1$  during four nights in March/April 2005. The derotator optical assembly was set to keep the pixel pattern stationary in equatorial coordinates at an angle of  $20^{\circ}$  clockwise relative to the axis of right ascension, so that the central row of pixels was aligned with the major axis of the molecular ring with the two molecular lobes being covered by two adjacent pixels (Fig. 1) and the third pixel pointing at a position  $24''$  southwest of the SW lobe. In this arrangement, the remaining pixels of the array pointed towards six positions  $24''$  northwest and southeast of the major axis (Fig. 2). The spectra were obtained in a wobbler switching mode with a beam throw of  $240''$  in azimuth. As backend, we used the WILMA autocorrelator, which provides a bandwidth of 1024 MHz (512 channels) in each of its 18 units. Having tuned the receivers to a rest frequency of 218.48 GHz at a velocity of  $200 \text{ km s}^{-1}$ , each bandpass thus covered simultaneously the para-H<sub>2</sub>CO ( $3_{03} \rightarrow 2_{02}$ ), ( $3_{22} \rightarrow 2_{21}$ ) and ( $3_{21} \rightarrow 2_{20}$ ) transitions (see Table 1). Good winter weather conditions resulted in system temperatures of 200 to 400 K ( $T_A^*$ ) and a pointing accuracy of  $3''$  or better. The chopper wheel calibration was checked by observing the C<sup>18</sup>O( $2 \rightarrow 1$ ) line at 219.56 GHz toward the reference source CLR 2688 and the relative stability of each tuning was determined by observing the H<sub>2</sub>CO emission of NGC 2264 IR and

DR21 OH. Both checks suggest a calibration uncertainty of less than 15%. The temperature scale was converted to main-beam brightness temperature ( $T_{\text{mb}}$ ) adopting a main beam efficiency of  $B_{\text{eff}} = 0.55$  and a forward efficiency of  $F_{\text{eff}} = 0.90$ .

The para- $\text{H}_2\text{CO}(2_{02} \rightarrow 1_{01})$  spectra at 145.60 GHz were obtained at the IRAM 30-m telescope during two days in August 2006. Using the wobbler switching mode (200" throw) of the new control system (NCS), we observed each molecular lobe in M82 with receivers C150 and D150 tuned to the same frequency and each connected to two parts of the 1 MHz filterbank, resulting in a bandwidth of 512 MHz with a channel spacing of 1 MHz for each receiver. During the observations, the system temperature was 200 to 350 K and the pointing was accurate within 3" to 4". Daily observations of the galactic sources W51E1 and/or W3OH suggest a calibration uncertainty of 10% or less. For the conversion of the antenna temperature to main-beam brightness temperature ( $T_{\text{mb}}$ ) a main beam efficiency of  $B_{\text{eff}} = 0.69$  and a forward efficiency of  $F_{\text{eff}} = 0.93$  were adopted.

## 2.2. Observations with the JCMT

During four shifts in December 2004 and January 2005, the SW lobe of M82 was observed with the dual-mixer receiver B3 at the JCMT<sup>2</sup> tuned to a rest frequency of 364.1 GHz and a velocity of  $180 \text{ km s}^{-1}$ . The observations were carried out in beam switching mode with a throw of 210". The DAS autocorrelator provided a bandwidth of 920 MHz with a spectral channel separation of 1.25 MHz in each of its two receiver channels, sufficient to cover simultaneously the para- $\text{H}_2\text{CO}$  transitions ( $5_{24} \rightarrow 4_{23}$ ), ( $5_{41} \rightarrow 4_{40}$ ) and ( $5_{42} \rightarrow 4_{41}$ ) as well as the ortho- $\text{H}_2\text{CO}$  transitions ( $5_{33} \rightarrow 4_{32}$ ) and ( $5_{32} \rightarrow 4_{31}$ ) (see Table 1). The system temperatures during the four shifts varied from  $\sim 750 \text{ K}$  to  $\sim 1650 \text{ K}$  and the uncertainty of the chopper wheel calibration was about 15% as indicated by observations of the standard source IRC+10216. The temperature scale was converted to main-beam brightness temperature using a beam efficiency of  $B_{\text{eff}} = 0.63$ .

---

<sup>2</sup>Program ID M04BC10; the James Clerk Maxwell Telescope is operated by The Joint Astronomy Centre on behalf of the Science and Technology Facilities Council of the United Kingdom, the Netherlands Organisation for Scientific Research, and the National Research Council of Canada.

### 2.3. Data Reduction

All data were reduced, converted to the main-beam temperature scale and analyzed using the GILDAS software package CLASS. Each individual spectrum was inspected for bad channels, standing waves or other baseline problems before a linear baseline was subtracted. The spectra at each position were then weighted according to their noise level, combined and smoothed to a common velocity resolution of  $10 \text{ km s}^{-1}$ . The data obtained at 218 GHz with the newly commissioned WILMA backend required special attention, because a large fraction of the individual spectra showed baseline problems ranging from prominent DC offsets to subtle ripples in certain sections of the bandpass. As a first step, the spectra were sorted into different groups according to their baseline quality. In order to guard against more subtle baseline problems compromising the determination of line strengths, we then fitted the lines in each individual spectrum using the multi-line fit of the corresponding combined spectrum (Section 3) as a template. When we selected only the spectra with the best baseline quality, representing  $\sim 40\%$  of the data, the  $\chi^2$ -tests yielded an agreement between the distribution of the fitted intensities and the expected Gaussian distribution at a 95% confidence level for each line in the spectra. The uncertainty of each fitted line intensity shown in Table 2 is the uncertainty in the mean of the Gaussian distribution  $\sigma_{\langle I \rangle} = \sigma_I / \sqrt{N}$  with  $\sigma_I$  the standard deviation of the Gaussian distribution and  $N$  the number of selected spectra.

## 3. RESULTS

We have detected the  $\text{H}_2\text{CO}(2_{02} \rightarrow 1_{01})$  line at 146 GHz as well as the transitions  $\text{H}_2\text{CO}(3_{03} \rightarrow 2_{02})$ ,  $\text{H}_2\text{CO}(3_{22} \rightarrow 2_{21})$  and  $\text{H}_2\text{CO}(3_{21} \rightarrow 2_{20})$  at 218 GHz in both molecular lobes of M 82. This constitutes the first detection of  $\text{H}_2\text{CO}(3_{22} \rightarrow 2_{21})$  emission from an external galaxy. We did not detect any  $\text{H}_2\text{CO}$  lines at 364 GHz, probably because of the limited sensitivity of our observations. The spectra of the molecular lobes and the fitted Gaussian lines are displayed in Fig. 3. The basic assumption that the observed lines are all emitted from the same volume of molecular gas with the same average physical properties implies that all lines should have the same velocity profile, parametrized in a Gaussian fit by the central velocity and the line width. Therefore we fixed the velocity and line width of all spectral features to the values derived from simultaneously fitting all the lines in the 218 GHz spectra. The derived velocities and widths in the two lobes are in very good agreement with the results of a fit to the strong  $\text{H}_2\text{CO}(3_{03} \rightarrow 2_{02})$  line alone. The parameters of the Gaussian fits and the resulting integrated intensities are summarized in Table 2.

The 218 GHz spectrum of the SW lobe is reproduced well by the three  $\text{H}_2\text{CO}$  lines near this frequency. The central velocity is  $132 \text{ km s}^{-1}$  (local standard of rest, hereafter LSR); the

line width is  $111 \text{ km s}^{-1}$ . In the spectrum of the NE lobe, the central velocity is  $301 \text{ km s}^{-1}$  (LSR) and the line width is  $131 \text{ km s}^{-1}$ . The apparent shift of the  $\text{H}_2\text{CO}(3_{22} \rightarrow 2_{21})$  line relative to the central velocity indicates the presence of at least one additional emission line, which we identify as the methanol  $\text{CH}_3\text{OH}(4_2 \rightarrow 3_1 E)$  transition at 218.44 GHz. The ratio of the fitted intensities of the highly blended lines  $\text{H}_2\text{CO}(3_{22} \rightarrow 2_{21})$  and  $\text{CH}_3\text{OH}(4_2 \rightarrow 3_1 E)$  can vary strongly with slight changes in the central velocity or the line width, which suggests that the fitting procedure is strongly influenced by the noise in the spectra. In addition, there might be faint  $\text{HC}_3\text{N}(24 \rightarrow 23)$  emission at 218.33 GHz in the spectrum of the NE lobe. However, the effect of such an additional component on the other fitted Gaussians is well inside the observational errors and can be neglected. The integrated line intensities resulting from a simultaneous fit of all five emission lines are given in parentheses in Table 2. A simultaneous fit of all five lines to the spectrum of the SW lobe gives a stringent upper limit to the  $\text{HC}_3\text{N}(24 \rightarrow 23)$  emission at this position.

In the SW lobe, the two  $\text{H}_2\text{CO}$  lines ( $3_{03} \rightarrow 2_{02}$ ) and ( $2_{02} \rightarrow 1_{01}$ ), detected with high signal-to-noise ratios, show a similar deviation from a Gaussian profile. They are skewed, with a blue-shifted peak and a weaker red line wing. The peak at  $v \sim 100 \text{ km s}^{-1}$  may originate from a gas component that has been identified previously in interferometric maps and may constitute the eastern part of the molecular super-shell (Weiß et al. 1999). To better account for these line profiles, we fitted two velocity components, a “narrow” one at  $\sim 100 \text{ km s}^{-1}$  and a “wide” one, to each identified spectral line using the velocity and line width derived from the  $\text{H}_2\text{CO}(3_{03} \rightarrow 2_{02})$  line (Table 2, Fig. 4). While the line profiles of the two strongest lines are fitted reliably by those two components, the result for the much weaker  $\text{H}_2\text{CO}(3_{21} \rightarrow 2_{20})$  line may be dominated by noise.

We also inspected the spectra obtained with the other pixels of the HERA array in order to search for possible outflows. Filaments of SiO emission, another molecule related to dust-chemistry and shocks, have been found at a distance as large as  $24''$  from the central plane (Fig. 2). No significant  $\text{H}_2\text{CO}$  emission was found in any of these spectra above a noise level of  $\sim 2 \text{ mK}$  (on the  $T_{\text{mb}}$  scale). Note, however, that  $\text{H}_2\text{CO}$  filaments may be present in the halo at locations not covered by our observations.

In both 146 GHz spectra, the  $\text{H}_2\text{CO}(2_{02} \rightarrow 1_{01})$  line at 145.60 GHz is partially blended with the  $\text{HC}_3\text{N}(16 \rightarrow 15)$  line at 145.56 GHz, but the two lines can easily be separated given the constraints derived from the 218 GHz spectra (Table 2). We did not detect any  $\text{H}_2\text{CO}$  emission at 364 GHz from the SW lobe. The values given in Table 2 are  $3\sigma$  upper limits, derived from the rms noise with the assumption that these lines have the same width and central velocity as those at 218 and 146 GHz.

## 4. DISCUSSION

### 4.1. The Physical Conditions of the Dense Molecular Gas

For the analysis of the derived integrated line intensities, we have developed a non-LTE code for para-H<sub>2</sub>CO adopting the Large Velocity Gradient (LVG) approximation and choosing a spherically symmetric cloud geometry. The choice of a particular cloud geometry can affect the resulting gas densities. In the LVG approximation, the escape probability  $\beta_{ij}$  for a photon of a transition  $ij$  is  $\beta_{ij} = (1 - \exp(-\tau_{ij})) \tau_{ij}^{-1}$  for a model with spherically symmetric geometry compared to  $\beta_{ij} = (1 - \exp(-3\tau_{ij})) (3\tau_{ij})^{-1}$  for a plane-parallel geometry. Thus, applying a plane-parallel instead of a spherical cloud geometry, photon trapping sets in at lower optical depths. In the optically thick case, the particle densities derived from the observed line ratios can be lower by up to half an order of magnitude (e.g. Ward et al. 2003). Our code is based on the collision rates with He by Green (1991), the collision rates with H<sub>2</sub> being approximated by a scaling factor of 1.37 (Schöier et al. 2005), and includes 41 para-H<sub>2</sub>CO levels, up to 210 cm<sup>-1</sup> (300 K) above the ground state. We checked our code successfully by using the physical conditions derived in this study as input to the on-line version of RADEX<sup>3</sup>, a program using a similar non-LTE code, and by comparing its output with our observed and derived line ratios and optical depths.

The velocity profiles of the two strong lines H<sub>2</sub>CO(2<sub>02</sub> → 1<sub>01</sub>) and H<sub>2</sub>CO(3<sub>03</sub> → 2<sub>02</sub>) are very similar in each lobe, suggesting that the H<sub>2</sub>CO emission is likely confined to a region within the smallest beam of the observations (11"). Interferometric maps of the integrated intensities of molecular transitions like CO(2 → 1), HCO<sup>+</sup>(1 → 0) and HCO( $F = 2 \rightarrow 1$ ) (e.g. Seaquist et al. 1998; Weiß et al. 2001b; García-Burillo et al. 2002) indicate that the NE and the SW lobes can be approximated by circular Gaussian distributions of 7" to 8" in diameter (FWHM). Here we adopt a Gaussian source distribution with a size of  $\theta_s = 7''.5$ , unless noted otherwise, and convolve all intensities to a common resolution of 17". We calculated the expected line ratios for a large number of physical conditions, covering the parameter space for a kinetic temperature of  $T_{\text{kin}} = 5$  to 300 K in steps of 5 K, a molecular gas density of  $\log n_{\text{H}_2} = 3.0$  to 6.0 (in cm<sup>-3</sup>) in steps of 0.1 and a para-H<sub>2</sub>CO column density per velocity interval of  $\log N_{\text{pH}_2\text{CO}}/\Delta v = 10.5$  to 14.5 (in cm<sup>-2</sup> km<sup>-1</sup> s) in steps of 0.1. The assumed ambient radiation field is the cosmic background radiation field ( $T_{\text{bg}} = 2.73$  K). Since the H<sub>2</sub>CO(3<sub>22</sub> → 2<sub>21</sub>) line in the NE lobe is heavily blended with a nearby methanol line (see Section 5) and does not add significant constraints to the physical conditions, we do not include the line in our LVG analysis for either lobe.

---

<sup>3</sup><http://www.strw.leidenuniv.nl/~moldata/>

Comparing the computed line ratios with our observational result (Table 3), we can significantly constrain the range of possible physical conditions in the molecular lobes of M82<sup>4</sup>. Note that in reality, the molecular gas is likely to be inhomogeneous in its properties such as temperature and density. However, given the limited number of measurements, we are constrained to consider only a one-component model, yielding the average properties of the molecular gas phase traced by H<sub>2</sub>CO.

The observed integrated line intensity of extragalactic sources is usually only a small fraction of the intensity predicted by the LVG calculations. This fraction  $F = T_{\text{obs}}/T_{\text{LVG}}$ , the so-called filling factor or dilution factor, is the product of several components  $F = f_b f_a f_v$  and provides insights into the structure of the observed source. The beam filling factor  $f_b = \theta_s^2 (\theta_s^2 + \theta_b^2)^{-1}$  accounts for the fact that the source does not extend over the whole beam area. Assuming a source size of  $\theta_s = 7''.5$ ,  $f_b = 0.163$  for a beam width of  $\theta_b = 17''$ . At the distance of M82 of  $D = 3.9$  Mpc (Sakai & Madore 1999), a  $17''$  beam covers an area with a diameter of 320 pc. Thus, it is reasonable to assume that the observed emission does not originate from a single molecular cloud, but rather represents an ensemble of giant molecular clouds, a giant molecular association. The individual clouds are expected to have (much) smaller radii than the overall source size and (much) smaller line widths than the observed beam-averaged width. Measures of this small-scale structure are the area filling factor  $f_a = C r^2 R_s^{-2}$  and the velocity filling factor  $f_v = \Delta v_{\text{cloud}} \Delta v_{\text{line}}^{-1}$ , where  $r$  and  $\Delta v_{\text{cloud}}$  are the radius and velocity width of an individual cloud,  $R_s$  is the radius of the source,  $\Delta v_{\text{line}}$  is the observed line width, and  $C$  is the total number of clouds in the beam. Since the latter two filling factors can not be separated, we combine them into the small-scale dilution factor  $F_{sc} = f_a f_v$ . Note that  $F_{sc}$  represents the volume filling factor of the velocity cube and thus can not be larger than unity.

Previous studies of H<sub>2</sub>CO emission in starburst galaxies suggest total H<sub>2</sub>CO abundances of the order of  $\sim 10^{-9}$  to  $\sim 10^{-8}$  (Hüttemeister et al. 1997; Wang et al. 2004; Martín et al. 2006b). In the high-temperature limit, the ortho-to-para-H<sub>2</sub>CO ratio is  $o/p = 3$ . However, in starburst galaxies,  $o/p$  may be closer to 1 or 2 (e.g. Hüttemeister et al. 1997). Adopting a para-H<sub>2</sub>CO abundance per velocity gradient of

$$\Lambda = \frac{X_{\text{pH}_2\text{CO}}}{\text{grad}(v)} = \frac{N_{\text{pH}_2\text{CO}}/\Delta v}{n_{\text{H}_2}} = 1 \times 10^{-9} \text{ km}^{-1} \text{ s pc},$$

---

<sup>4</sup>Splitting the observed H<sub>2</sub>CO line profiles in the SW lobe into two velocity components (Table 2), the H<sub>2</sub>CO(2<sub>02</sub> → 1<sub>01</sub>)/H<sub>2</sub>CO(3<sub>03</sub> → 2<sub>02</sub>) line ratio suggests that the narrow component has a higher density than the wide component at a given abundance per velocity gradient and kinetic temperature. However, since the other line ratios are highly uncertain because of the low signal-to-noise ratio in the H<sub>2</sub>CO(3<sub>21</sub> → 2<sub>20</sub>) line, we do not treat the two velocity component separately in the following analysis.

we derive the physical conditions of the molecular gas in the lobes by comparing the observed line ratios (Table 3,  $\theta_s = 7''.5$ ) with those calculated in the model parameter space. While inter-ladder line ratios of formaldehyde are generally good tracers of the kinetic temperature and intra-ladder ratios sensitively trace the density at a given temperature (Section 1.1), we find that at moderate gas densities of  $\sim 10^4 \text{ cm}^{-3}$  and high kinetic temperatures of  $> 100 \text{ K}$ , the individual line ratios are not completely independent of the other model parameters and that a combination of the line ratios constrains the physical properties of the molecular gas even more tightly. Figure 5 shows the cuts through the parameter space where the different derived line ratios intersect. Also plotted are the uncertainties given in Table 3. We derive similar physical conditions for the two lobes, in particular a high kinetic temperature of  $\sim 200 \text{ K}$  and a moderate gas density of  $n_{\text{H}_2} \sim 7.4 \times 10^3 \text{ cm}^{-3}$  (Table 4). Under these conditions, the 146 GHz line is optically thick, while the optical depth of the 218 GHz lines is of the order of unity and the emission at 364 GHz is optically thin.

If the line width  $v_{\text{cloud}}$  of an individual cloud is dominated by its velocity gradient ( $\Delta v_{\text{cloud}} \approx 2r \text{ grad}(v)$ ) and the clouds are close to virial equilibrium, a cloud gas density of  $n_{\text{H}_2} = 7.4 \times 10^3 \text{ cm}^{-3}$  suggests a velocity gradient of  $\text{grad}(v) \approx 1.0 \text{ km s}^{-1} \text{ pc}^{-1}$ , which is in very good agreement with the velocity gradient deduced from high-resolution CO observations (Weiß et al. 2001b). In this case, the para-formaldehyde abundance is  $X_{\text{pH}_2\text{CO}} \approx 1 \times 10^{-9}$  and the total formaldehyde abundance  $X_{\text{H}_2\text{CO}} \approx 2$  to  $4 \times 10^{-9}$ , depending on the ortho-to-para formaldehyde ratio. The mass of the molecular clouds within the beam of the telescope is

$$\frac{M_{\text{mol}}}{M_{\odot}} = 6.828 \times 10^{-19} \frac{N_{\text{H}_2, \text{beam}}}{\text{cm}^{-2}} \left( \frac{D}{\text{Mpc}} \right)^2 \left( \frac{\theta_{\text{beam}}}{\text{arcsec}} \right)^2,$$

where  $N_{\text{H}_2, \text{beam}} = (N_{\text{pH}_2\text{CO}}/\Delta v) X_{\text{pH}_2\text{CO}}^{-1} \Delta v_{\text{line}} F$  is the beam-averaged  $\text{H}_2$  column density. This equation includes a factor 1.6 to account for dust and other molecular and atomic species like helium. At a distance of  $D = 3.9 \text{ Mpc}$  (Sakai & Madore 1999),  $M_{\text{mol}} = 1.7 \times 10^8 M_{\odot}$  in the NE lobe and  $M_{\text{mol}} = 1.4 \times 10^8 M_{\odot}$  in the SW lobe.

The small-scale dilution factor  $F_{sc} = F f_b^{-1}$  can be derived from our LVG calculations. Expressed in terms of cloud properties, it is

$$F_{sc} = f_a f_v = \frac{C r^2 \Delta v_{\text{cloud}}}{R_s^2 \Delta v_{\text{line}}}.$$

Assuming again that the line width of an individual cloud is dominated by its velocity gradient,

$$C r^3 = \frac{R_s^2 \Delta v_{\text{line}} F_{sc}}{2 \text{ grad}(v)},$$

yielding  $r = 34 C^{-1/3}$  pc in the NE lobe and  $r = 33 C^{-1/3}$  pc in the SW lobe for a velocity gradient of  $1 \text{ km s}^{-1} \text{ pc}^{-1}$ . For comparison, the maximum radius of a cloud is given by the observed line width and the velocity gradient  $r_{\text{max}} = \Delta v_{\text{line}} / (2 \text{ grad}(v)) = 66 \text{ pc}$  and  $56 \text{ pc}$  in the NE and SW lobes, respectively. The fraction of the volume that the molecular clouds occupy within the source is

$$\Phi = \frac{C (4/3) \pi r^3}{\pi R_s^2 l} = \frac{2 \Delta v_{\text{line}} F_{sc}}{3 \text{ grad}(v) l},$$

where  $l \approx 350 \text{ pc}$  is the adopted line of sight extent of the emitting region. For a gradient of  $1 \text{ km s}^{-1} \text{ pc}^{-1}$ ,  $\Phi \approx (0.30)^3$  or about 30% in each dimension of the data cube in both lobes. Thus, the observed volume could contain a small number of large clouds, whose diameters are comparable to the source size, or a large number of small clouds, but the presence of only a single cloud within the beam is ruled out.

The results for other choices of  $\Lambda$  can be found in Tables 5 and 6. In the optically thin limit (see e.g. models N1 and N2), the small-scale dilution factor reaches its maximum value of  $F_{sc} = 1$  and the temperature-density plots are almost independent of the assumed  $\text{H}_2\text{CO}$  column density per velocity interval. Thus, there is a lower limit to the kinetic temperatures and an upper limit to the gas densities consistent with our observations. We do not find a solution (corresponding to the intersection of the curves for the line ratios) in the calculated parameter space for  $T_{\text{kin}} \lesssim 140 \text{ K}$  (NE lobe) and  $T_{\text{kin}} \lesssim 155 \text{ K}$  (SW lobe), respectively. The upper limit to the gas density is  $n_{\text{H}_2} \sim 2.5 \times 10^4$  in both lobes.

The assumed source size  $\theta_s$  also has a significant influence on the derived parameters (Table 4). A larger source size results in a lower kinetic temperature, a higher  $\text{H}_2$  density and a smaller small-scale dilution factor. But even if the  $\text{H}_2\text{CO}$  emitting region is as large as  $10''$ , the kinetic temperature in the lobes is  $\sim 170 \text{ K}$ , which is much higher than the dust temperature of  $T_{\text{dust}} = 48 \text{ K}$  (Colbert et al. 1999) or the commonly assumed kinetic temperatures of  $30 \text{ K}$  to  $100 \text{ K}$ . To summarize, the dominant component of the molecular gas in the lobes of M 82 seems to be in a warm phase of moderate density.

## 4.2. Comparison with Other Excitation Studies

Numerous previous studies have used molecular lines to derive the physical properties of the molecular gas in M 82. Frequently, the small number of lines available to constrain

the free parameters has led to the adoption of a kinetic temperature of  $T_{\text{kin}} \sim 50$  K, similar to the dust temperature  $T_{\text{dust}} = 48$  K (Colbert et al. 1999). This assumption is supported by the results of early analyzes of the low- $J$  CO lines (e.g. Wild et al. 1992) and, more recently, by the ammonia study of Weiß et al. (2001a, see below).

The most comprehensive data base exists for CO and  $^{13}\text{CO}$  lines, which have been searched for up to  $J = 7 \rightarrow 6$  (Mao et al. 2000) and  $J = 6 \rightarrow 5$  (Ward et al. 2003), respectively. Based on this large collection of CO lines, Mao et al. (2000) confirm that a one-component LVG model can not fit all the observed line intensities simultaneously. Thus, in order to derive the properties of the high-excitation component, they restrict their LVG analysis to the high- $J$  excitation lines in the submm-range, i.e. CO( $7 \rightarrow 6$ ), CO( $4 \rightarrow 3$ ), CO( $3 \rightarrow 2$ ), and  $^{13}\text{CO}$ ( $3 \rightarrow 2$ ). In the most recent multi-line CO study, Ward et al. (2003) analyze the CO and  $^{13}\text{CO}$  emission at all available transitions using a two-component plane-parallel LVG model. The physical properties of the high-excitation molecular gas phase derived from these comprehensive excitation studies are compared to our results in Table 7. Considering that our investigation is completely independent of the other studies, the results are remarkably similar. The physical properties derived from our  $\text{H}_2\text{CO}$  data and our LVG model adopting a spherically symmetric cloud morphology lie well within the range of values found for the high-excitation component of the two-component LVG model by Ward et al. (2003). In fact, our kinetic temperature is only 20 K to 40 K higher than their median value, which is influenced by the limited temperature range considered, and their median density is lower by only a factor of  $\sim 2$  if the effect of using a plane-parallel model versus a spherically symmetric one is taken into account. The most striking difference between our results and the values derived by Mao et al. (2000) is their lower kinetic temperature. A possible explanation for this discrepancy is a small contribution of the cooler low-excitation component to the submm CO line emission that would lower the average kinetic temperature of the one-component model.

The presence of a warm gas component in nearby starburst galaxies with  $T_{\text{kin}} = 50$  to 440 K was also inferred from the detection of highly excited  $\text{NH}_3$  lines (Mauersberger et al. 2003). In this study, M82 was the notable exception in not showing evidence for a warm molecular gas component in its  $\text{NH}_3$  emission. The ammonia inversion lines detected towards M82 suggest a rotational temperature of only 29 K and thus a kinetic temperature of only  $\sim 60$  K in the SW lobe of M82 (Weiß et al. 2001a). In contrast, Rigopoulou et al. (2002) find a warm molecular gas component with  $T_{\text{kin}} \sim 150$  K in a sample of starburst and Seyfert galaxies including M82 by analyzing IR rotational  $\text{H}_2$  emission lines. Possible mechanisms that could heat a large fraction of the molecular gas to temperatures of  $\sim 150$  K include shocks, strong UV and/or X-ray irradiation (PDR, XDR) (e.g. Rigopoulou et al. 2002; Fuente et al. 2005) as well as the more uniform cosmic ray heating (Bradford et al.

2003), in short processes that are likely to be found in an active environment such as a starburst.

A comparison of the H<sub>2</sub>CO line widths and the derived molecular gas mass with the values derived from the CO studies suggests that the H<sub>2</sub>CO lines trace approximately the same gas as traced by the ubiquitous CO lines (Table 7). According to our data, each lobe contains warm molecular gas of about  $M_{\text{mol}} \sim 1.5 \times 10^8 M_{\odot}$ , which is in good agreement with the estimate by Mao et al. (2000) of  $M_{\text{mol}} \sim 1 - 10 \times 10^8 M_{\odot}$  and the mass of the molecular ring of  $M_{\text{mol}} \sim 2.0 \times 10^8 M_{\odot}$  derived by Ward et al. (2003) from the integrated intensity of their CO(6 → 5) map. Having modeled the physical conditions and the conversion factor  $X_{\text{CO}}$  at 18 positions along the circumnuclear ring as traced by high-resolution low-J CO maps, Weiß et al. (2001b) find a molecular gas mass of  $M_{\text{mol}} \sim 2.5 \times 10^8 M_{\odot}$  in the ring, whereas applying the standard conversion factor  $X_{\text{CO}} = 1.6 \times 10^{20} \text{ cm}^{-2} (\text{K km s}^{-1})^{-1}$  to their data leads to a total mass of  $M_{\text{mol}} \sim 7.1 \times 10^8 M_{\odot}$ .

In contrast to the results of the CO and H<sub>2</sub>CO investigations, the observed ammonia inversion lines seem to arise from cold, probably well shielded regions within the ISM (Mauersberger et al. 2003). The physical properties derived in our analysis and the CO studies suggest that the majority of the gas is in a warm state of comparatively low density ( $n_{\text{H}_2} \sim 7 \times 10^3 \text{ cm}^{-3}$ ), which fits well with the idea that M 82 is in an advanced phase of a starburst. In such an environment, ammonia is easily photodissociated outside of the few remaining well-shielded regions (Fuente et al. 1993), which may explain the extremely low NH<sub>3</sub> column densities reported by Weiß et al. (2001a).

## 5. METHANOL EMISSION FROM THE MOLECULAR LOBES OF M 82

The detection of the H<sub>2</sub>CO(3<sub>21</sub> → 2<sub>20</sub>) line in both molecular lobes strongly suggests that there is H<sub>2</sub>CO(3<sub>22</sub> → 2<sub>21</sub>) emission at these positions too. On the other hand, Martín et al. (2006a) very recently reported the detection of methanol emission from the lobes of M 82 including the highly excited 5<sub>k</sub> → 4<sub>k</sub> transition. Thus, it is reasonable to expect CH<sub>3</sub>OH(4<sub>2</sub> → 3<sub>1 E</sub>) emission to originate from the two lobes as well. As a result, the observed spectral features at 218.5 GHz in both lobes most likely consist of the strongly blended emission of the H<sub>2</sub>CO(3<sub>22</sub> → 2<sub>21</sub>) and the CH<sub>3</sub>OH(4<sub>2</sub> → 3<sub>1 E</sub>) lines at 218.48 GHz and at 218.44 GHz, respectively. Because of this blending, the spectral feature at ~ 218.5 GHz was ignored in the LVG analysis in Section 4.1. Now we can use the results of our LVG models to derive the expected strengths of the H<sub>2</sub>CO(3<sub>22</sub> → 2<sub>21</sub>) emission for different physical conditions (Tables 5 and 6). Interestingly, the computed values for each lobe vary by no more than 5% throughout the range of model parameters considered, which

indicates that the  $\text{H}_2\text{CO}(3_{22} \rightarrow 2_{21})$  emission does not add significant constraints to the LVG analysis, probably because the similar  $\text{H}_2\text{CO}(3_{21} \rightarrow 2_{20})$  line is already included. In order to deconvolve the highly blended lines, we fixed the integrated intensity of the  $\text{H}_2\text{CO}(3_{22} \rightarrow 2_{21})$  emission to the value derived from the models and fitted the five lines with the usual constraints (Table 2). Fig. 6 shows the resulting Gaussian fits and the residual spectra in both lobes. The derived integrated intensities are summarized in Table 8.

In the SW lobe, the  $\text{H}_2\text{CO}(3_{22} \rightarrow 2_{21})$  emission predicted by the LVG analysis agrees within  $3\sigma$  with the previously derived integrated intensity, and the estimated contribution of the methanol line is well below the uncertainty of the mean of the fitted  $\text{H}_2\text{CO}$  line. In the NE lobe, the methanol line appears to be about six times stronger, while the predicted  $\text{H}_2\text{CO}(3_{22} \rightarrow 2_{21})$  emission is comparable to that of the SW lobe. The noise level in the NE residual spectrum is slightly increased at the position of the subtracted blended lines. However, this is also the case at the position of the subtracted  $\text{H}_2\text{CO}(3_{03} \rightarrow 2_{02})$  line and may be due to a deviation of the line profile from a Gaussian shape. The result that the  $\text{CH}_3\text{OH}(4_2 \rightarrow 3_1 E)$  emission of the NE lobe is much stronger than that of the SW lobe agrees very well with the line strengths reported by Martín et al. (2006a). Their intensities of the blended methanol lines at 97 GHz and 157 GHz are similar in both lobes. However, the  $\text{CH}_3\text{OH}(5_k \rightarrow 4_k)$  transitions at 242 GHz, which require high excitation levels similar to those needed to observe the  $\text{CH}_3\text{OH}(4_2 \rightarrow 3_1 E)$  transition, are stronger in the NE lobe than in the SW lobe, which might indicate a difference in excitation.

## 6. CONCLUSIONS

1. We have detected several para- $\text{H}_2\text{CO}$  emission lines at 146 GHz and 218 GHz in both molecular lobes near the center of the nearby starburst galaxy M 82. To our knowledge, our study constitutes the first dedicated search for  $\text{H}_2\text{CO}$  transitions with  $K_a > 1$  and the first detection of  $\text{H}_2\text{CO}(3_{22} \rightarrow 2_{21})$  emission outside of the Galactic neighborhood.
2. Our line ratio analysis using an LVG model with spherical cloud symmetry suggests the presence of warm ( $T_{\text{kin}} \sim 200$  K), moderately dense ( $n_{\text{H}_2} \sim 7 \times 10^3 \text{ cm}^{-3}$ ) molecular gas in the lobes near the center of the starburst activity. The ratio of column density to volume density and the small small-scale filling factor may indicate that the observed molecular gas forms large complexes of comparatively low-density molecular gas, possibly extended envelopes around a few remaining well-shielded cores.
3. The physical properties of the molecular gas derived from our  $\text{H}_2\text{CO}$  data are in very good agreement with parameters of the high-excitation component in the lobes of M 82 found in recent comprehensive CO studies, but differ from the results of a multi-line

NH<sub>3</sub> investigation. Thus, the para-H<sub>2</sub>CO lines seem to trace the probably dominant high-excitation component of the molecular gas in M82 very well, while the NH<sub>3</sub> emission might originate predominantly from cold cloud cores.

4. The total mass of the molecular gas observed in the lobes is a few times  $10^8 M_{\odot}$ , similar to the mass determinations of other molecular line studies.
5. The selected para-H<sub>2</sub>CO transitions are good tracers of the molecular gas in starburst galaxies, even if a large fraction of the gas is in a warm phase ( $T_{\text{kin}} \sim 150$  K) of moderate density ( $n_{\text{H}_2} \lesssim 10^4 \text{ cm}^{-3}$ ).
6. We find strong evidence for CH<sub>3</sub>OH( $4_2 \rightarrow 3_1 E$ ) emission in the spectrum of the NE lobe at 218 GHz and also estimate the intensity of this emission line in the SW lobe. We thus confirm the detection of methanol in M82 by Martín et al. (2006b) with measurements of another transition line that are consistent with the earlier findings.

We wish to thank the staff at Pico Veleta/Granada and at the JCMT/MKSS/JAC for their support during the observations. We also thank the anonymous referee whose thoughtful comments greatly helped to improve the manuscript. S.M. acknowledges a travel grant from the Natural Science and Engineering Research Council of Canada (NSERC) administered by the National Research Council of Canada (NRC) for the observations at the JCMT. E.R.S. acknowledges a Discovery Grant from NSERC. This work has made use of the following software and resources: GILDAS, specx, Statistiklabor (FU Berlin, CeDiS), asyerr (Seaquist & Yao), the JPL Catalog of spectral lines, The Cologne Database for Molecular Spectroscopy (CDMS Müller et al. 2005) and NASA’s Astrophysics Data System Bibliographic Services (ADS).

*Facilities:* IRAM:30m (CD,HERA), JCMT (B3).

## REFERENCES

- Baan, W. A., Henkel, C., Schilke, P., Mauersberger, R., & Güsten, R. 1990, ApJ, 353, 132
- Benson, P. J., & Myers, P. C. 1983, ApJ, 270, 589
- Bradford, C. M., Nikola, T., Stacey, G. J., Bolatto, A. D., Jackson, J. M., Savage, M. L., Davidson, J. A., & Higdon, S. J. 2003, ApJ, 586, 891
- Charnley, S. B., Tielens, & A. G. G. M., Millar, T. J. 1992, ApJ, 399, L71

- Colbert, J. W., et al. 1999, *ApJ*, 511, 721
- Fuente, A., García-Burillo, S., Gerin, M., Rizzo, J. R., Usero, A., Teyssier, D., Roueff, E., & Le Boulrot, J. 2006, *ApJ*, 641, L105
- Fuente, A., García-Burillo, S., Gerin, M., Teyssier, D., Usero, A., Rizzo, J. R., & De Vicente, P. 2005, *ApJ*, 619, L155
- Fuente, A., Martín-Pintado, J., Cernicharo, J., & Bachiller, R. 1993, *A&A*, 276, 473
- García-Burillo, S., Martín-Pintado, J., Fuente, A., Usero, A., Neri, R. 2002, *ApJ*, 575, L55
- García-Burillo, S., Martín-Pintado, J., Fuente, A., & Neri, R. 2001, *ApJ*, 563, L27
- Gardner, F. F., & Whiteoak, J. B. 1974, *Nature*, 247, 526
- Graham, D. A., Emerson, D. T., Weiler, K. W., Wielebinski, R., & de Jager, G. 1978, *A&A*, 70, L69
- Green, S. 1991, *ApJS*, 76, 979
- Heikkilä, A., Johansson, L. E. B., & Olofsson, H. 1999, *A&A*, 344, 817
- Hüttemeister, S., Mauersberger, R., & Henkel, C. 1997, *A&A*, 326, 59
- Johansson, L. E. B., Olofsson, H., Hjalmarsen, A., Gredel, R., & Black, J. H. 1994, *A&A*, 291, 89
- Johnstone, D., Boonman, A. M. S., & van Dishoeck, E. F. 2003, *A&A*, 412, 157
- Klessen, R. S., Spaans, M., & Jappsen, A. K. 2007, *MNRAS*, 374, L29
- Mangum, J. G., & Wootten, A. 1993, *ApJS*, 89, 123
- Mao, R. Q., Henkel, C., Schulz, A., Zielinsky, M., Mauersberger, R., Störzer, H., Wilson, T. L., & Gensheimer, P. 2000, *A&A*, 358, 433
- Martín, S., Martín-Pintado, J., & Mauersberger, R. 2006a, *A&A*, 450, L13
- Martín, S., Mauersberger, R., Martín-Pintado, J., Henkel, C., & García-Burillo, S. 2006b, *ApJS*, 164, 450
- Mauersberger, R., Henkel, C., & Wilson, T. L. 1987, *A&A*, 173, 352
- Mauersberger, R., Henkel, C., Weiß, A., Peck, A. B., & Hagiwara, Y. 2003, *A&A*, 403, 561

- Müller, H. S. P., Schlöder, F., Stutzki, J., & Winnewisser, G. 2005, *J. Mol. Struct.* 742, 215
- Paumard, T., et al. 2006, *ApJ* 643, 1011
- Rigopoulou, D., Kunze, D., Lutz, D., Genzel, R., & Moorwood, A. F. M. 2002, *A&A*, 389, 374
- Sakai, S., & Madore, B. F. 1999, *ApJ*, 526, 599
- Schöier, F. L., van der Tak, F. F. S., van Dishoeck, & E. F., Black, J. H. 2005, *A&A*, 432, 369
- Seaquist, E. R., & Bell, M. B. 1990, *ApJ*, 364, 94
- Seaquist, E. R., Frayer, D. T., & Bell, M. B. 1998, *ApJ*, 507, 745
- Seaquist, E. R., Lee, S. W., & Moriarty-Schieven, G. H. 2006, *ApJ*, 638, 148
- Wang, M., Henkel, C., Chin, Y.-N., Whiteoak, J. B., Hunt Cunningham, M., Mauersberger, R., & Muders, D. 2004, *A&A*, 422, 883
- Watanabe, N., & Kouchi, A. 2002, *ApJ*, 571, L173
- Ward, J. S., Zmuidzinas, J., Harris, A. I., & Isaak, K. G. 2003, *ApJ*, 587, 171
- Weiß, A., Neininger, N., Henkel, C., Stutzki, J., & Klein, U. 2001a, *ApJ*, 554, L143
- Weiß, A., Neininger, N., Hüttemeister, S., & Klein, U. 2001b, *A&A*, 365, 571
- Weiss, A., Walter, F., Neininger, N., & Klein, U., 1999, *A&A*, 345, L23
- Wild, W., Harris, A. J., Eckart, A., Genzel, R., Graf, U. U., Jackson, J. M., Russell, A. P. G., & Stutzki, J. 1992, *A&A*, 265, 447

Table 1. Summary of the observed para- (*p*) and ortho-H<sub>2</sub>CO (*o*) transitions.

Transition		$\nu$ /[GHz]	$\theta_b^a$ /["]	rms <sup>b</sup> /[mK]
H <sub>2</sub> CO(2 <sub>02</sub> → 1 <sub>01</sub> )	<i>p</i>	145.6029	17	1.9, 1.8
H <sub>2</sub> CO(3 <sub>03</sub> → 2 <sub>02</sub> )	<i>p</i>	218.2222	11	2.7, 2.4
H <sub>2</sub> CO(3 <sub>22</sub> → 2 <sub>21</sub> )	<i>p</i>	218.4756	11	2.7, 2.4
H <sub>2</sub> CO(3 <sub>21</sub> → 2 <sub>20</sub> )	<i>p</i>	218.7601	11	2.7, 2.4
H <sub>2</sub> CO(5 <sub>24</sub> → 4 <sub>23</sub> )	<i>p</i>	363.9459	13	5.4, n/a
H <sub>2</sub> CO(5 <sub>42</sub> → 4 <sub>41</sub> )	<i>p</i>	364.1032	13	5.4, n/a
H <sub>2</sub> CO(5 <sub>41</sub> → 4 <sub>40</sub> )	<i>p</i>	364.1032	13	5.4, n/a
H <sub>2</sub> CO(5 <sub>33</sub> → 4 <sub>32</sub> )	<i>o</i>	364.2751	13	5.4, n/a
H <sub>2</sub> CO(5 <sub>32</sub> → 4 <sub>31</sub> )	<i>o</i>	364.2889	13	5.4, n/a

<sup>a</sup>half power beam width (FWHM)

<sup>b</sup>rms in  $T_{\text{mb}}$  at 10 km s<sup>-1</sup> resolution at the positions of the SW lobe and the NE lobe, respectively

Table 2. Input parameters and results of the Gaussian fits to the observed emission lines.

Parameter	NE lobe	SW lobe	SW lobe/narrow	SW lobe/wide
$v_0$ [km s <sup>-1</sup> ]	301.0 ± 3.6	132.2 ± 4.8	106.3 ± 5.8	174.3 ± 12.7
$\Delta v_{\text{line}}$ [km s <sup>-1</sup> ]	130.7 ± 4.1	111.2 ± 6.4	48.3 ± 10.5	77.1 ± 18.6
$\int T_{\text{mb}} dv(\text{H}_2\text{CO}(2_{02} \rightarrow 1_{01}))$	3.69 ± 0.10	2.76 ± 0.10	1.34 ± 0.07	1.60 ± 0.15
$\int T_{\text{mb}} dv(\text{HC}_3\text{N}(16 \rightarrow 15))$	0.46 ± 0.11	0.70 ± 0.09	< 0.19	0.42 ± 0.08
$\int T_{\text{mb}} dv(\text{H}_2\text{CO}(3_{03} \rightarrow 2_{02}))$	2.75 ± 0.18 (2.73)	2.09 ± 0.16 (2.09)	0.98 ± 0.08	1.10 ± 0.12
$\int T_{\text{mb}} dv(\text{H}_2\text{CO}(3_{22} \rightarrow 2_{21}))$	<i>0.05 ± 0.17 (0.11)</i>	<i>1.09 ± 0.15 (1.10)</i>	<i>0.57 ± 0.08</i>	<i>0.41 ± 0.10</i>
$\int T_{\text{mb}} dv(\text{H}_2\text{CO}(3_{21} \rightarrow 2_{20}))$	0.67 ± 0.15 (0.68)	0.53 ± 0.14 (0.53)	0.25 ± 0.09	0.21 ± 0.08
$\int T_{\text{mb}} dv(\text{CH}_3\text{OH}(4_2 \rightarrow 3_1 E))$	<i>1.45 ± 0.21 (1.39)</i>	(< 0.27)		
$\int T_{\text{mb}} dv(\text{HC}_3\text{N}(24 \rightarrow 23))$	(0.17)	(< 0.27)		
$\int T_{\text{mb}} dv(\text{H}_2\text{CO}(5_{24} \rightarrow 4_{23}))$		< 0.54		
$\int T_{\text{mb}} dv(\text{H}_2\text{CO}(5_{4x} \rightarrow 4_{4y}))^{\text{a}}$		< 0.54		
$\int T_{\text{mb}} dv(\text{H}_2\text{CO}(5_{3x} \rightarrow 4_{3y}))^{\text{b}}$		< 0.54		

<sup>a</sup>integrated intensity of the highly blended lines H<sub>2</sub>CO(5<sub>42</sub> → 4<sub>41</sub>) and H<sub>2</sub>CO(5<sub>41</sub> → 4<sub>40</sub>)

<sup>b</sup>integrated intensity of the highly blended lines H<sub>2</sub>CO(5<sub>33</sub> → 4<sub>32</sub>) and H<sub>2</sub>CO(5<sub>32</sub> → 4<sub>31</sub>)

Note. — All integrated intensities in K km s<sup>-1</sup> (main-beam temperature scale) and before correction for beam width. The last two columns show the line intensities in the SW lobe that result from the assumption of two velocity components (“narrow” and “wide”). At each position, the velocity  $v_0$ , the line width  $\Delta v_{\text{line}}$  and their errors were derived by simultaneously fitting Gaussians with a fixed frequency offset and the same (unknown) line width to the detected lines in the 218 GHz spectrum (NE lobe: 4 components, SW lobe: 3 components, SW lobe/narrow and wide: 2 components to the H<sub>2</sub>CO(3<sub>03</sub> → 2<sub>02</sub>) line alone). The derived velocities and line widths were then fixed for the fits to the other spectra. Values in parentheses show the results of a simultaneous fit to all five potentially present lines in the 218 GHz spectra (H<sub>2</sub>CO(3<sub>03</sub> → 2<sub>02</sub>), HC<sub>3</sub>N(24 → 23), CH<sub>3</sub>OH(4<sub>2</sub> → 3<sub>1 E</sub>), H<sub>2</sub>CO(3<sub>22</sub> → 2<sub>21</sub>), and H<sub>2</sub>CO(3<sub>21</sub> → 2<sub>20</sub>)); values in italics indicate highly blended lines, whose fit is uncertain; upper limits in this table are 3 $\sigma$  limits to the integrated intensities of the spectral lines using the adopted line widths.

Table 3. Beam-corrected line ratios derived from the observed line intensities and the assumed source size  $\theta_s$

line intensity ratio / source, $\theta_s^a$	NE, 5''	NE, 7''5	NE, 10''	SW, 5''	SW, 7''5	SW, 10''
$\text{H}_2\text{CO}(2_{02} \rightarrow 1_{01})/\text{H}_2\text{CO}(3_{03} \rightarrow 2_{02})$	$2.88^{+0.20}_{-0.22}$	$2.61^{+0.18}_{-0.20}$	$2.36^{+0.16}_{-0.18}$	$2.84^{+0.23}_{-0.26}$	$2.58^{+0.21}_{-0.24}$	$2.33^{+0.19}_{-0.21}$
$\text{H}_2\text{CO}(2_{02} \rightarrow 1_{01})/\text{H}_2\text{CO}(3_{21} \rightarrow 2_{20})$	$11.91^{+2.21}_{-3.11}$	$10.79^{+1.99}_{-2.81}$	$9.75^{+1.80}_{-2.54}$	$11.26^{+2.31}_{-3.31}$	$10.20^{+2.09}_{-3.00}$	$9.22^{+1.89}_{-2.71}$
$\text{H}_2\text{CO}(3_{03} \rightarrow 2_{02})/\text{H}_2\text{CO}(3_{21} \rightarrow 2_{20})$	$4.13^{+0.80}_{-1.12}$	$4.13^{+0.80}_{-1.12}$	$4.13^{+0.80}_{-1.12}$	$3.96^{+0.85}_{-1.21}$	$3.96^{+0.85}_{-1.21}$	$3.96^{+0.85}_{-1.21}$
$\text{H}_2\text{CO}(2_{02} \rightarrow 1_{01})/\text{H}_2\text{CO}(5_{24} \rightarrow 4_{23})$				$> 8.28$	$> 7.84$	$> 7.40$

<sup>a</sup>selected lobe, assumed source size  $\theta_s$

Table 4. Results of our LVG calculations and the derived physical properties assuming  $\Lambda = 1 \times 10^{-9} \text{ km}^{-1} \text{ s pc}$ .

parameter / source, $\theta_s$ <sup>a</sup>	NE, 5''	NE, 7''5	NE, 10''	SW, 5''	SW, 7''5	SW, 10''
$T_{\text{kin}}$ [K]	230	191	161	256	209	181
$\log n_{\text{H}_2}$ [ $\text{cm}^{-3}$ ]	3.67	3.87	4.04	3.67	3.87	4.02
$\log N_{\text{pH}_2\text{CO}}/\Delta v$ <sup>b</sup> [ $\text{cm}^{-2} \text{ km}^{-1} \text{ s}$ ]	13.16	13.36	13.53	13.16	13.36	13.51
$\tau_{145.6}$ <sup>c</sup>	2.508	3.628	4.306	2.473	3.551	4.173
$\tau_{218.2}$ <sup>c</sup>	0.636	1.345	1.933	0.642	1.355	1.943
$\tau_{218.5}$ <sup>c</sup>	0.261	0.432	0.520	0.274	0.455	0.557
$\tau_{218.8}$ <sup>c</sup>	0.153	0.273	0.343	0.163	0.291	0.368
$\tau_{364.0}$ <sup>c</sup>	0.003	0.007	0.010	0.004	0.008	0.011
$F$ <sup>c,d</sup>	0.025	0.019	0.013	0.037	0.018	0.013
$F_{sc}$ <sup>c,e</sup>	0.24	0.11	0.08	0.23	0.11	0.08
$p = n_{\text{H}_2} T_{\text{kin}}$ [ $10^6 \text{ cm}^{-3} \text{ K}$ ]	1.1	1.4	1.8	1.2	1.6	1.9
$N_{\text{pH}_2\text{CO,beam}}$ <sup>f</sup> [ $10^{13} \text{ cm}^{-2}$ ]	4.7	5.7	5.8	6.0	4.6	4.7
$N_{\text{H}_2,\text{beam}}$ <sup>g</sup> [ $10^{22} \text{ cm}^{-2}$ ]	4.7	5.7	5.8	6.0	4.6	4.7
$M_{\text{mol}}$ <sup>h</sup> [ $10^8 M_{\odot}$ ]	1.4	1.7	1.7	1.8	1.4	1.4

<sup>a</sup>selected lobe, assumed source size  $\theta_s$

<sup>b</sup>calculated from  $\Lambda$  and  $\log n_{\text{H}_2}$

<sup>c</sup>evaluated at the nearest grid point

<sup>d</sup>dilution factor  $F = T_{\text{obs}}/T_{\text{lvg}}$  in a 17'' beam; the 218 GHz data are scaled to a 17'' beam assuming a source size of  $\theta_s$

<sup>e</sup>small-scale dilution factor  $F_{sc} = F f_b^{-1} = f_a f_v = F/0.163$  for  $\theta_s = 7''5$ .

<sup>f</sup>beam-averaged column density  $N_{\text{pH}_2\text{CO,beam}} = (N_{\text{pH}_2\text{CO}}/\Delta v) \Delta v_{\text{line}} F$

<sup>g</sup>beam-averaged column density, assuming  $X_{\text{pH}_2\text{CO}} = 1 \times 10^{-9}$

<sup>h</sup>molecular gas mass, assuming  $X_{\text{pH}_2\text{CO}} = 1 \times 10^{-9}$  and  $D = 3.9 \text{ Mpc}$

Table 5. Results of our LVG calculations for various physical conditions of the molecular gas in the NE lobe.

model	$T_{\text{kin}}$ [K]	$\log n_{\text{H}_2}$ [ $\text{cm}^{-3}$ ]	$\log N_{\text{pH}_2\text{CO}}/\Delta v$ [ $\text{cm}^{-2} \text{km}^{-1} \text{s}$ ]	$X_{\text{pH}_2\text{CO}}/\text{grad } v$ [ $10^{-9} \text{km}^{-1} \text{s pc}$ ]	$\tau_{146}^{\text{a}}$	$\tau_{218.2}^{\text{a}}$	$\tau_{218.5}^{\text{a}}$	$\tau_{218.8}^{\text{a}}$	$\tau_{364}^{\text{a}}$	$F^{\text{a},\text{b}}$	$F_{\text{sc}}^{\text{a},\text{c}}$	$\int T_{\text{mb}} dv_{218.5}^{\text{a},\text{d}}$ [K km s $^{-1}$ ]
T1	150	4.24	12.73	0.100	0.78	0.22	0.09	0.06	0.002	0.059	0.36	0.53
T2	175	4.02	13.18	0.469	2.41	0.79	0.29	0.18	0.006	0.027	0.16	0.54
T3	200	3.79	13.47	1.55	4.72	1.81	0.53	0.33	0.008	0.020	0.12	0.55
T4	225	3.64	13.61	3.03	6.24	2.23	0.58	0.34	0.007	0.023	0.14	0.55
T5	250	3.52	13.75	5.51	9.52	4.02	0.84	0.51	0.010	0.017	0.11	0.54
T6	275	3.40	13.88	9.81	11.96	5.24	0.95	0.59	0.010	0.016	0.10	0.55
T7	300	3.28	13.99	16.65	15.07	6.82	1.11	0.67	0.011	0.016	0.10	0.55
N1	142	4.38	12.00	0.0135	0.15	0.04	0.19	0.13	0.0007	0.202	1.24	n/a <sup>e</sup>
N2	146	4.31	12.50	0.0503	0.49	0.14	0.06	0.04	0.002	0.078	0.48	0.52
N3	159	4.13	13.00	0.2407	1.54	0.46	0.19	0.12	0.004	0.036	0.22	0.53
N4	206	3.76	13.50	1.7842	4.68	1.81	0.53	0.33	0.008	0.020	0.12	0.55
N5	298	3.28	14.00	17.0392	15.04	6.80	1.11	0.67	0.011	0.016	0.10	0.55

Note. — For the T models, a kinetic temperature was specified, while the N models used a specific para-H<sub>2</sub>CO column density per velocity interval as an input parameter.

<sup>a</sup>evaluated at the nearest grid point

<sup>b</sup>dilution factor  $F = T_{\text{obs}}/T_{\text{lvg}}$  in a 17'' beam; the 218 GHz data are scaled to a 17'' beam assuming a source size of  $\theta_s = 7''.5$

<sup>c</sup>small-scale dilution factor  $F_{\text{sc}} = F f_b^{-1} = f_a f_v = F/0.163$  for  $\theta_s = 7''.5$ .

<sup>d</sup>calculated integrated intensity of the H<sub>2</sub>CO(3<sub>21</sub> → 2<sub>20</sub>) line

<sup>e</sup>value ambiguous

Table 6. Results of our LVG calculations for various physical conditions of the molecular gas in the SW lobe.

model	$T_{\text{kin}}$ [K]	$\log n_{\text{H}_2}$ [ $\text{cm}^{-3}$ ]	$\log N_{\text{pH}_2\text{CO}}/\Delta v$ [ $\text{cm}^{-2} \text{ km}^{-1} \text{ s}$ ]	$X_{\text{pH}_2\text{CO}}/\text{grad } v$ [ $10^{-9} \text{ km}^{-1} \text{ s pc}$ ]	$\tau_{146}^{\text{a}}$	$\tau_{218.2}^{\text{a}}$	$\tau_{218.5}^{\text{a}}$	$\tau_{218.8}^{\text{a}}$	$\tau_{364}^{\text{a}}$	$F^{\text{a},\text{b}}$	$F_{\text{sc}}^{\text{a},\text{c}}$	$\int T_{\text{mb}} dv_{218.5}^{\text{a},\text{d}}$ [K km s $^{-1}$ ]
T2	175	4.17	12.83	0.148	0.943	0.287	0.130	0.085	0.004	0.038	0.23	0.42
T3	200	3.93	13.28	0.727	3.014	1.024	0.366	0.230	0.006	0.022	0.13	0.43
T4	225	3.78	13.45	1.52	4.605	1.832	0.561	0.354	0.009	0.016	0.10	0.43
T5	250	3.65	13.60	2.89	5.790	2.393	0.671	0.423	0.010	0.015	0.09	0.43
T6	275	3.53	13.72	5.03	7.726	2.948	0.717	0.432	0.008	0.018	0.11	0.43
T7	300	3.43	13.86	8.74	11.78	5.282	1.022	0.625	0.011	0.014	0.08	0.43
N1	159	4.34	12.00	0.0148	0.153	0.041	0.020	0.014	0.0006	0.203	1.25	0.41
N2	164	4.27	12.50	0.0551	0.472	0.140	0.065	0.044	0.002	0.064	0.39	0.42
N3	183	4.10	13.00	0.2579	1.492	0.470	0.201	0.130	0.005	0.029	0.18	0.43
N4	230	3.75	13.50	1.8258	4.575	1.827	0.564	0.358	0.009	0.016	0.10	0.43

Note. — For the T models, a kinetic temperature was specified, while the N models used a specific para-H<sub>2</sub>CO column density per velocity interval as an input parameter.

<sup>a</sup>evaluated at the nearest grid point

<sup>b</sup>dilution factor  $F = T_{\text{obs}}/T_{\text{lvg}}$  in a 17'' beam; the 218 GHz data are scaled to a 17'' beam assuming a source size  $\theta_s = 7''.5$

<sup>c</sup>small-scale dilution factor  $F_{\text{sc}} = F f_b^{-1} = f_a f_v$

<sup>d</sup>calculated integrated intensity of the H<sub>2</sub>CO(3<sub>21</sub> → 2<sub>20</sub>) line

Table 7. Comparison of our results to those of other excitation studies.

parameter/study	our data (NE/SW)	Ward/median (NE/SW) <sup>a,b</sup>	Ward/range (NE/SW) <sup>a,c</sup>	Mao (NE/SW) <sup>d</sup>
$\theta_b$ [arcsec]	17	24.4	24.4	22
$\Delta v_{\text{line}}$ [km s <sup>-1</sup> ]	131/111	180/160	180/160	$\sim 120/\sim 130^e$
$T_{\text{kin}}$ [K]	191/209	170/170	$> 50/> 50$	60 – 130
$n_{\text{H}_2}$ [10 <sup>3</sup> cm <sup>-3</sup> ]	7.4/7.4	0.6/1.0	0.3 – 100/0.3 – 20	2.0 – 7.9
$N_{\text{H}_2,\text{beam}}$ [10 <sup>22</sup> cm <sup>-2</sup> ]	5.7/4.6	1.3/1.0	0.08 – 5.0/0.16 – 12.6	$\sim 10$
$M_{\text{mol}}$ [10 <sup>8</sup> $M_{\odot}$ ]	1.7/1.4	2.0 <sup>f,g</sup>		1 – 10 <sup>g</sup>

<sup>a</sup>high-excitation component of a two-component LVG model assuming a plane-parallel geometry, using all available CO and <sup>13</sup>CO lines; for a spherical model,  $n_{\text{H}_2} \sim 5$  times larger,  $N_{\text{H}_2} \sim 2$  times larger and  $T_{\text{kin}}$  better constrained and slightly lower (Ward et al. 2003)

<sup>b</sup>median likelihood of possible values, not a self-consistent solution

<sup>c</sup>full range of possible values (95% confidence interval)

<sup>d</sup>one-component LVG model assuming a spherically symmetric cloud geometry, using only the high-excitation lines CO(7 → 6), CO(4 → 3), CO(3 → 2), and <sup>13</sup>CO(3 → 2) (Mao et al. 2000)

<sup>e</sup>FWHM, derived from CO(2 → 1) and CO(1 → 0) spectra

<sup>f</sup>using the average CO column density derived from the integrated CO(6 → 5) intensity map

<sup>g</sup>scaled to a distance of  $D = 3.9$  Mpc, assumed to be the total mass

Table 8. Derived integrated intensities of the emission lines at 218.5 GHz at 11'' resolution.

	NE lobe	SW lobe
$\int T_{\text{mb}} dv(\text{H}_2\text{CO}(3_{22} \rightarrow 2_{21}))_{\text{models}}$ [K km s <sup>-1</sup> ]	1.07	0.84
$\int T_{\text{mb}} dv(\text{CH}_3\text{OH}(4_2 \rightarrow 3_1 E))_{\text{fitted}}$ [K km s <sup>-1</sup> ]	0.61	0.10
$3\sigma$ [K km s <sup>-1</sup> ]	0.26	0.27
residual noise level at 218.5 GHz [mK]	3.0 <sup>a</sup>	2.3
rms noise level over the whole baseline [mK]	2.4	2.7

<sup>a</sup>for comparison, the residual noise level at the position of the H<sub>2</sub>CO(3<sub>03</sub> → 2<sub>02</sub>) line is 3.3 mK

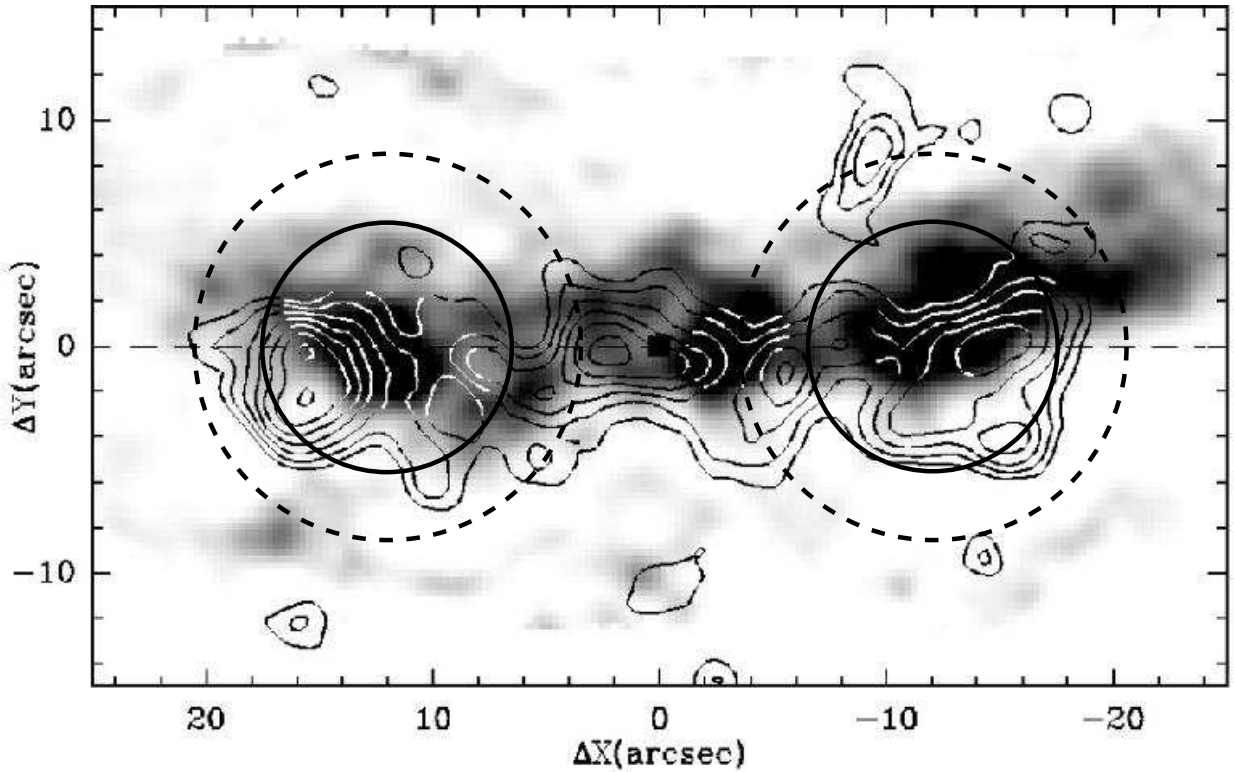


Fig. 1.— Contours of the  $\text{HCO}(F = 2 \rightarrow 1)$  emission superposed on a high-resolution  $\text{CO}(2 \rightarrow 1)$  map of the molecular ring in M82 adapted from García-Burillo et al. (2002). Map offsets are relative to the dynamical center of the galaxy ( $\alpha_{2000} = 09^{\text{h}}55^{\text{m}}51^{\text{s}}.9$ ,  $\delta_{2000} = 69^{\circ}40'47''.1$ ) with the x-axis along the plane of the molecular ring (P.A.=  $70^{\circ}$  east of north). The observed pointing positions and the corresponding beam widths are marked by the solid ( $11''$  at 218 GHz) and the dashed ( $17''$  at 146 GHz) circles.

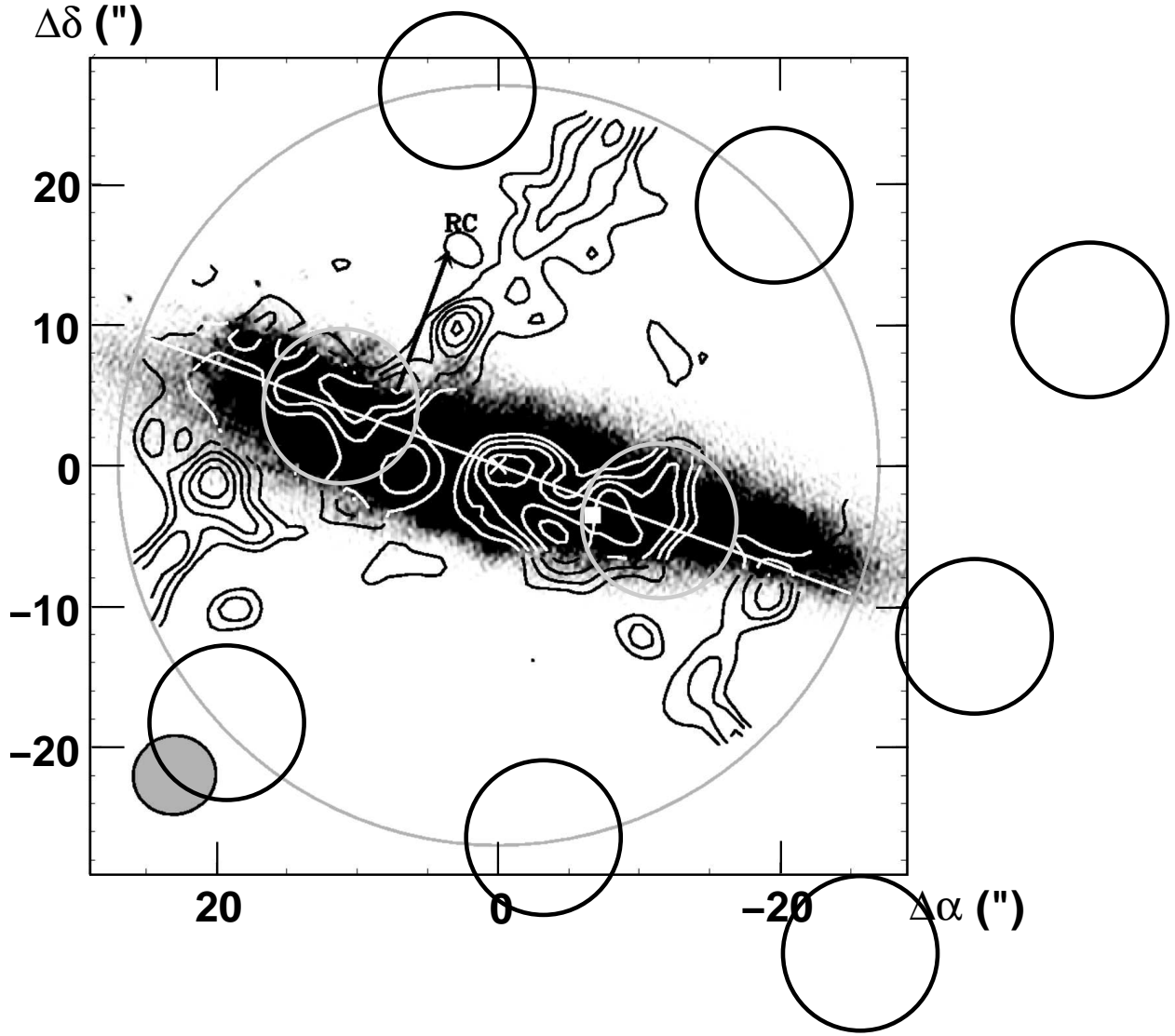


Fig. 2.— Contours of the velocity-integrated SiO( $v = 0$ ,  $J = 2 - 1$ ) emission superposed on a radio continuum emission image at 4.8 GHz, adapted from García-Burillo et al. (2001). Map offsets are relative to the dynamical center of the galaxy ( $\alpha_{2000} = 09^{\text{h}}55^{\text{m}}51^{\text{s}}.9$ ,  $\delta_{2000} = 69^{\circ}40'47''.1$ ). The large circle delimits the primary beam field of the SiO interferometric observations at 87 GHz ( $55''$ ), while the synthesized beam is shown in the bottom left corner. The white square marks the position of SNR 41.95+57.5. The radio continuum filament is indicated by an arrow. The pointing positions observed with the HERA array and the beam width of  $11''$  are marked by the gray and black solid circles, where the gray circles cover the molecular lobes in M 82.

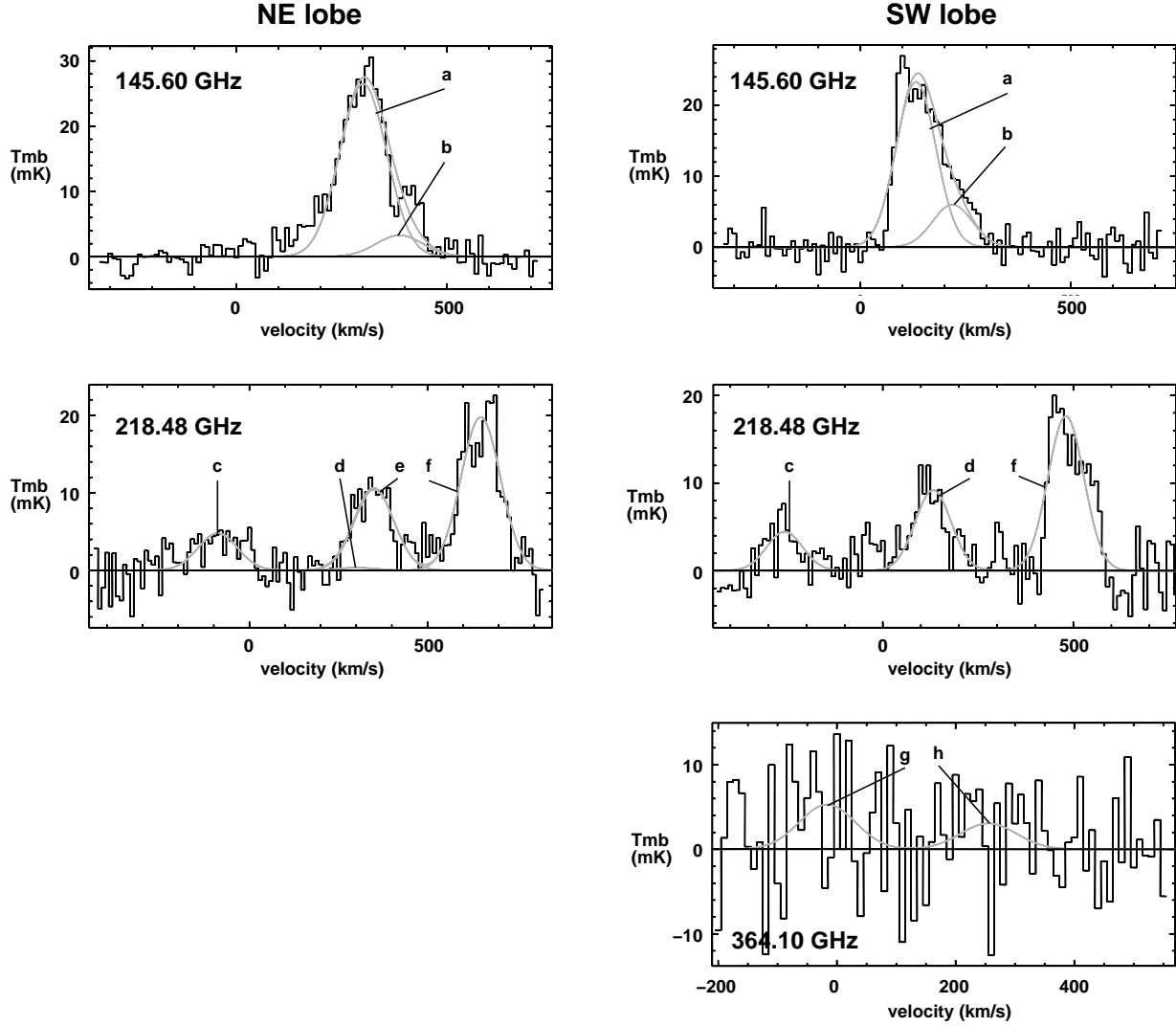


Fig. 3.— Observed spectra of the NE (left) and the SW lobe (right) of M82. Each spectrum is labeled with the frequency the receiver was tuned to. Thus, the velocity scale of the 218.48 GHz spectra refers to the  $\text{H}_2\text{CO}(3_{22} \rightarrow 2_{21})$  line. The  $\text{H}_2\text{CO}(3_{03} \rightarrow 2_{02})$  and the  $\text{H}_2\text{CO}(3_{21} \rightarrow 2_{20})$  transitions are offset by  $348.5 \text{ km s}^{-1}$  and  $-389.7 \text{ km s}^{-1}$ , respectively, while the  $\text{CH}_3\text{OH}(4_2 \rightarrow 3_1 E)$  line is offset by  $49.4 \text{ km s}^{-1}$ . In the 146 GHz spectra, the  $\text{HC}_3\text{N}(16 \rightarrow 15)$  line is offset by  $86.46 \text{ km s}^{-1}$  from the  $\text{H}_2\text{CO}(2_{02} \rightarrow 1_{01})$  emission. Gaussian line profiles were fitted to every individual line assuming the same line width and velocity for all lines. All identified lines of a spectrum were fitted simultaneously with these constraints. The curves show the Gaussian fit to each individual line as well as the spectrum resulting from a superposition of all identified lines: a =  $\text{H}_2\text{CO}(2_{02} \rightarrow 1_{01})$ , b =  $\text{HC}_3\text{N}(16 \rightarrow 15)$ , c =  $\text{H}_2\text{CO}(3_{21} \rightarrow 2_{20})$ , d =  $\text{H}_2\text{CO}(3_{22} \rightarrow 2_{21})$ , e =  $\text{CH}_3\text{OH}(4_2 \rightarrow 3_1 E)$ , f =  $\text{H}_2\text{CO}(3_{03} \rightarrow 2_{02})$ , g =  $\text{H}_2\text{CO}(5_{33} \rightarrow 4_{32}) + \text{H}_2\text{CO}(5_{32} \rightarrow 4_{31})$ , h =  $\text{H}_2\text{CO}(5_{24} \rightarrow 4_{23})$ .

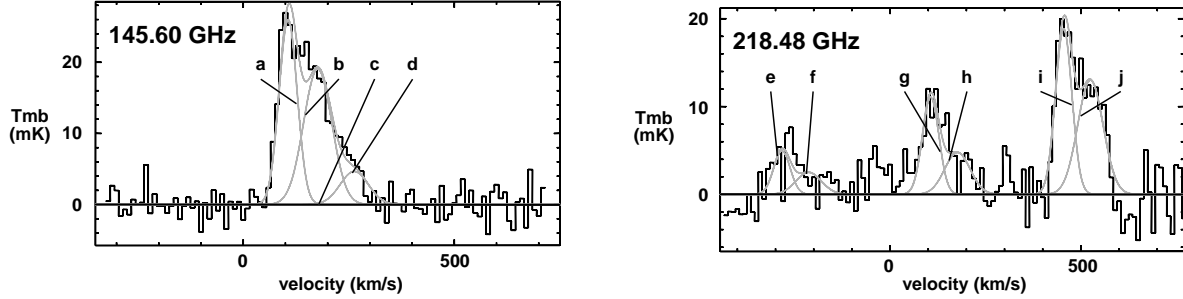


Fig. 4.— Spectra of the SW lobe observed at 146 GHz (left) and 218 GHz (right). To better match the observed line profiles, two velocity components ( $v_1$  and  $v_2$ ) with a mutual separation of  $68 \text{ km s}^{-1}$  were fitted to each previously identified line. The curves show the Gaussian fit to each individual line as well as the spectrum resulting from a superposition of all identified lines: a =  $\text{H}_2\text{CO}(2_{02} \rightarrow 1_{01})_{v1}$ , b =  $\text{H}_2\text{CO}(2_{02} \rightarrow 1_{01})_{v2}$ , c =  $\text{HC}_3\text{N}(16 \rightarrow 15)_{v1}$ , d =  $\text{HC}_3\text{N}(16 \rightarrow 15)_{v2}$ , e =  $\text{H}_2\text{CO}(3_{21} \rightarrow 2_{20})_{v1}$ , f =  $\text{H}_2\text{CO}(3_{21} \rightarrow 2_{20})_{v2}$ , g =  $\text{H}_2\text{CO}(3_{22} \rightarrow 2_{21})_{v1}$ , h =  $\text{H}_2\text{CO}(3_{22} \rightarrow 2_{21})_{v1}$ , i =  $\text{H}_2\text{CO}(3_{03} \rightarrow 2_{02})_{v1}$ , j =  $\text{H}_2\text{CO}(3_{03} \rightarrow 2_{02})_{v2}$ . Note that the  $\text{H}_2\text{CO}(2_{02} \rightarrow 1_{01})_{v2}$  and the  $\text{HC}_3\text{N}(16 \rightarrow 15)_{v1}$  lines are strongly blended with a separation in velocity of only  $16.5 \text{ km s}^{-1}$ .

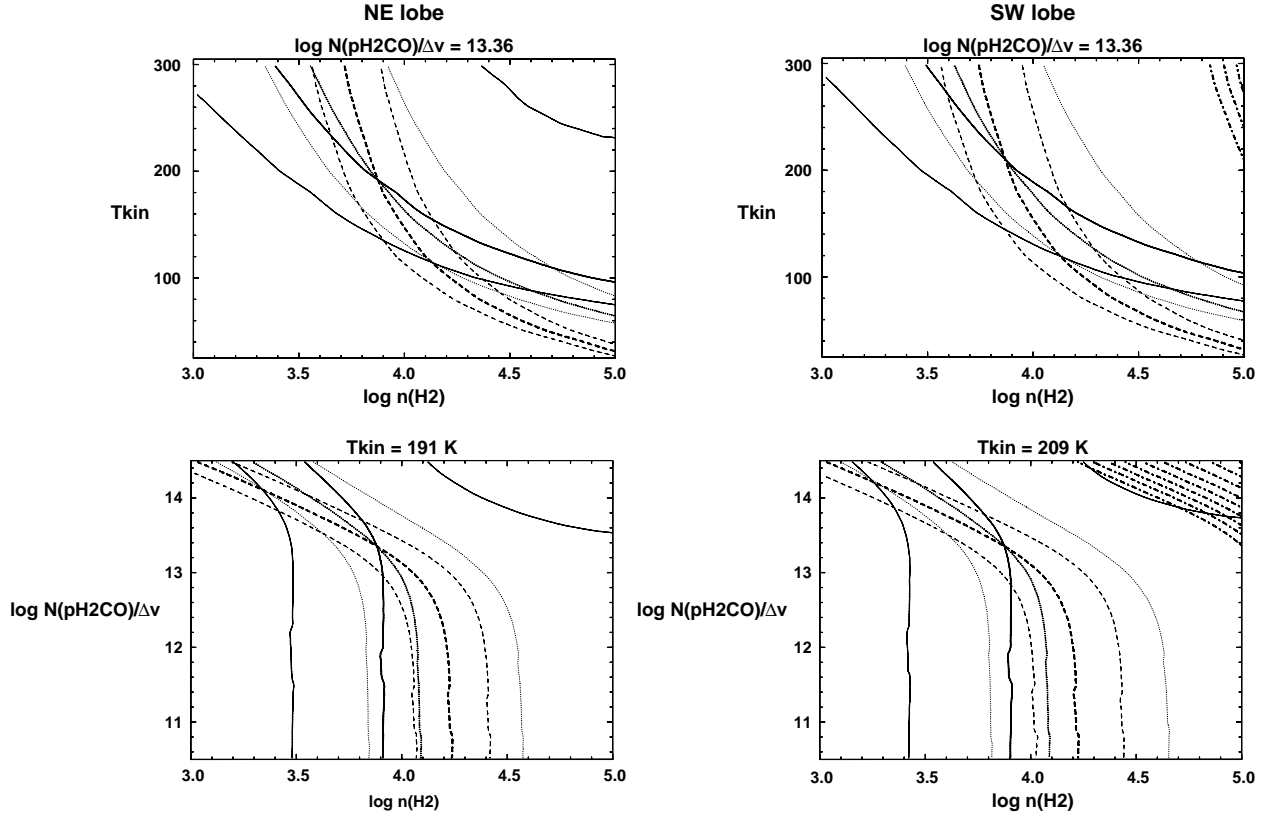


Fig. 5.— Results of our LVG analysis for the NE and SW lobes shown as cuts through the 3-D parameter space ( $T_{\text{kin}}$  in K,  $n_{\text{H}_2}$  in  $\text{cm}^{-3}$ ,  $N_{\text{pH}_2\text{CO}}/\Delta v$  in  $\text{cm}^{-2} \text{km}^{-1} \text{s}$ ) along a plane of constant para- $\text{H}_2\text{CO}$  column density per velocity interval (top) and of constant kinetic temperature (bottom). The thick lines represent the following line ratios:  $\text{H}_2\text{CO}(3_{03} \rightarrow 2_{02})/\text{H}_2\text{CO}(3_{21} \rightarrow 2_{20})$  (solid),  $\text{H}_2\text{CO}(2_{02} \rightarrow 1_{01})/\text{H}_2\text{CO}(3_{03} \rightarrow 2_{02})$  (dashed),  $\text{H}_2\text{CO}(2_{02} \rightarrow 1_{01})/\text{H}_2\text{CO}(3_{21} \rightarrow 2_{20})$  (dotted). The thin lines outline the corresponding uncertainties given in Table 3. The dashed-dotted line in the plots for the SW lobe denotes the area that is ruled out by the lower limit to the line ratio of  $\text{H}_2\text{CO}(2_{02} \rightarrow 1_{01})/\text{H}_2\text{CO}(5_{24} \rightarrow 4_{23})$ . The adopted source size is  $\theta_s = 7''.5$  and the assumed para- $\text{H}_2\text{CO}$  abundance per velocity gradient is  $\Lambda = 1 \times 10^{-9} \text{km}^{-1} \text{s pc}$ .

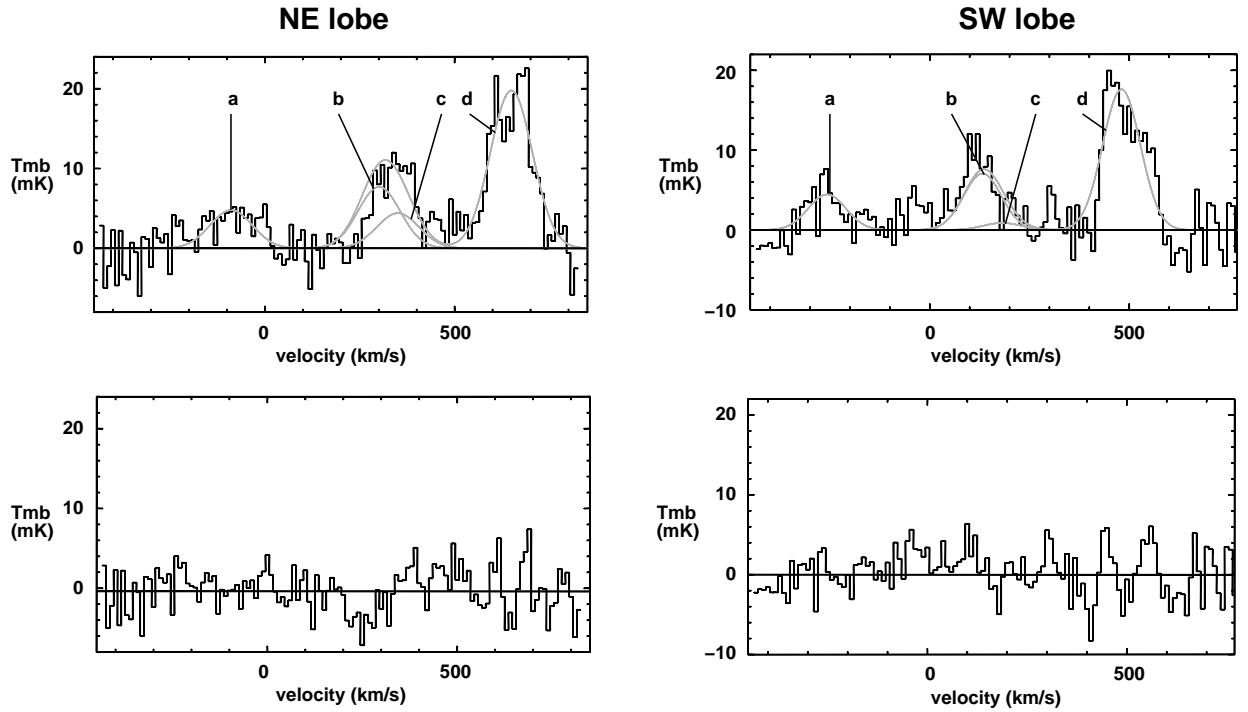


Fig. 6.— **Top:** Gaussian fits derived from the LVG analysis (Section 5) superposed on the 218 GHz spectra of the NE lobe (left) and the SW lobe (right); the curves show the Gaussian fit to each individual line as well as the spectrum resulting from a superposition of all identified lines: a =  $\text{H}_2\text{CO}(3_{21} \rightarrow 2_{20})$ , b =  $\text{H}_2\text{CO}(3_{22} \rightarrow 2_{21})$ , c =  $\text{CH}_3\text{OH}(4_2 \rightarrow 3_1 E)$ , d =  $\text{H}_2\text{CO}(3_{03} \rightarrow 2_{02})$ . **Bottom:** Residual spectra after subtraction of the Gaussian fits.